Understanding dynamics of the system using Hilbert phases: An application to study neonatal and fetal brain signals

R. B. Govindan,[1] S. Vairavan,[2] J. D. Wilson,[2] H. Preissl,[3] J. Vrba,[4] C. L. Lowery,[1] and H. Eswaran[1]

[1]*Department of Obstetrics and Gynecology, University of Arkansas for Medical Sciences, Little Rock, Arkansas 72205, USA*
[2]*Graduate Institute of Technology, University of Arkansas at Little Rock, Little Rock, Arkansas 72204, USA*
[3]*MEG Center, University of Tuebingen, 72076 Tuebingen, Germany*
[4]*Elekta-Neuromag Oy, 00530 Helsinki, Finland*

The Hilbert phase $\phi(t)$ of a signal $x(t)$ exhibits slips when the magnitude of their successive phase difference $|\phi(t_{i+1}) - \phi(t_i)|$ exceeds π. By applying this approach to periodic, uncorrelated, and long-range correlated data, we show that the standard deviation of the time difference between the successive phase slips $\Delta\tau$ normalized by the percentage of slips in the data is characteristic of the correlation in the data. We consider a 50×50 square lattice and model each lattice point by a second-order autoregressive (AR2) process. Further, we model a subregion of the lattice using a different set of AR2 parameters compared to the rest. By applying the proposed approach to the lattice model, we show that the two distinct parameter regions introduced in the lattice are clearly distinguishable. Finally, we demonstrate the application of this approach to spatiotemporal neonatal and fetal magnetoencephalography signals recorded using 151 superconducting quantum interference device sensors to identify the sensors containing the neonatal and fetal brain signals and discuss the improved performance of this approach over the traditionally used spectral approach.

I. INTRODUCTION

A model free time series analysis [1] approach is suited to characterize the dynamics of a system without the knowledge of the underlying details of the dynamical equation. In most applications, the main objective of time series analysis is to classify the system into one of its possible different dynamical states. Here, we propose a method based on Hilbert phase to characterize the dynamics of the system. Practically, there are several advantages in characterizing the signal by studying the phases rather than the amplitude since the phase is always bounded between $-\pi$ and π. Several bivariate and multivariate analyses based on Hilbert phase have been introduced to understand the nature of coupling between two or more signals [2–4]. Further, several univariate approaches based on the phase of a signal have been proposed to study the synchrony between two or more systems [5,6]. The investigation of synchrony between the signals from their phases, especially in spatiotemporal systems [7], localizes the connection-interaction better than the conventional coherence measure as the latter suffers due to the mixing property [8] (a property related to smearing of amplitude of a region to neighboring regions). In this work, we perform a univariate analysis of the Hilbert phase of a signal. Precisely, we characterize the dynamics of the signal by the standard deviation of the time difference between the consecutive phase slips that occur when the magnitude of the phase difference exceeds the value of π and normalize this quantity by the percentage of slips in the given data.

The paper is organized as follows: in Sec. II we explain the procedure of phase slip analysis using a sine wave; we demonstrate the application of this approach in characterizing white noise and long-range correlated noise and show that the Hilbert phase is characteristic of the correlations in the data. In this work, we plan to use this approach to iden-

tify the neonatal and fetal brain signals embedded in high-dimensional data. Prior to this, we test it by simulating a lattice and modeling each lattice point by a second-order autoregressive (AR2) process. By applying the current approach to AR2 lattice, we show that the phase slip analysis correctly distinguishes the two distinct parameter regions incorporated in the lattice. Finally, using this approach we identify the neonatal and fetal brain signals embedded in spatiotemporal magnetoencephalographic (MEG) data measured using a 151 superconducting quantum interference device (SQUID) system.

II. METHODOLOGY OF PHASE SLIP ANALYSIS

A. Hilbert transform and Hilbert phase

To demonstrate the methodology of phase slip analysis, we consider a sine wave, $x(t) = \sin(2\pi t/40)$, sampled at 4 Hz for a period of 100 s. For the signal $x(t)$ the Hilbert transform $h(t)$ is defined by the following convolution integral:

$$h(t) = \frac{1}{\pi} P \int_{-\infty}^{\infty} \frac{x(\tau)}{t - \tau} d\tau, \tag{1}$$

where P denotes Cauchy's principal value. The signal together with its Hilbert transform can be represented as a complex analytic signal $a(t) = x(t) + ih(t)$, where $i = \sqrt{-1}$. Using the complex signal $a(t)$, the Hilbert phase is defined as $\phi(t) = \tan^{-1}\{h(t)/x(t)\}$ and thus Hilbert transform allows us to study the instantaneous phase of the signal. Though Hilbert transform based approach is commonly used to capture the phase of a signal, another definition also exists to quantify the phase. If the trajectories (irrespective of whether they are obtained by the numerical simulation of the dynamical equations or reconstructed from the time series) of a dynamical system display rotations in the phase space, then one can

define an appropriate plane and study the crossing of the trajectories with the plane. Based on the time between successive crossings, one can define the phase of the trajectory. This approach is used to study the phase synchronization in low-dimensional chaotic system [9–11]. However, for biological signals such as neonatal and fetal brain waves as studied in this work may not confine to a low-dimensional phase space and hence it will be difficult to define the phase using this approach. Therefore, in this work we define the phase using the Hilbert transform approach. However, all the different approaches capture the instantaneous period of the dynamics.

B. Generalized Hilbert transform

The convolution integral Eq. (1) basically introduces a phase shift of $-\pi/2$ to the signal $x(t)$. That is, if we represent the Fourier transform $[P_x(\omega)]$ of $x(t)$ as $r(\omega)e^{i\omega t}$ then the Fourier transform $[P_h(\omega)]$ of $h(t)$ will be $r(\omega)e^{i(\omega t - \pi/2)}$. Based on this relation, one can numerically compute $h(t)$ retrospectively by introducing a desired phase shift of $-\pi/2$ to the Fourier phases of the original signal.

This definition can further be generalized by introducing any desired phase shift c to the Fourier phases of the given signal $x(t)$ as follows: $\widehat{h(t)} = F^{-1}\{P_x(\omega)e^{i(\omega t + c)}\}$, where $F^{-1}\{\cdot\}$ denotes the inverse Fourier transform operation. We define $\widehat{h(t)}$ as the generalized Hilbert transform of the signal $x(t)$ and if c takes on a value of $-\pi/2$, $\widehat{h(t)}$ becomes equal to $h(t)$. Numerically, one can compute $\widehat{h(t)}$ by multiplying the Fourier phases of a signal with desired phase shift e^{ic}. To this end, an inverse Fourier transform is applied to bring the signal back to time domain.

C. Characterization of phase slips

Based on the above arguments, the Hilbert transform of $\sin(2\pi t/40)$ is $\sin(2\pi t/40 - \pi/2) = -\cos(2\pi t/40)$. Thus, for a sine wave with frequency ω, the Hilbert phase can be determined analytically $\phi(t) = \omega t - \pi/2$.

In this work, $a(n)$ is computed numerically using the "Hilbert" function in MATLAB (Mathworks Inc., Natick, MA, USA), where $t = n/s$ and s is sample frequency and n is the sample number. A portion of the simulated sine wave and the Hilbert phase $\phi(t)$ are shown in Fig. 1. The time difference between the successive phase slips $\tau^{(1)}$ is also shown in Fig. 1. In order to better understand this result, we consider the phases computed for the case $c = \pi$. It is easy to infer from the above definition of $\widehat{h(t)}$ that this value of the phase shift will flip the signal polarity and the analytic signal will be $a(t) = x(t) - ix(t)$. The corresponding Hilbert phase and the time between the successive phase slips $\tau^{(2)}$ are also presented in Fig. 1. For the case $c = -\pi/2$, the phase slip occurs when the signal passes through a minimum and for $c = \pi$ the phase slip occurs when the signal passes through zero. Thus, the Hilbert transform with a phase shift of π can be thought of as a zero-crossing detector which is traditionally used in signal processing to capture the dominant frequency of the signal [12]. Further, for the case of $-\pi/2$ the phase slip
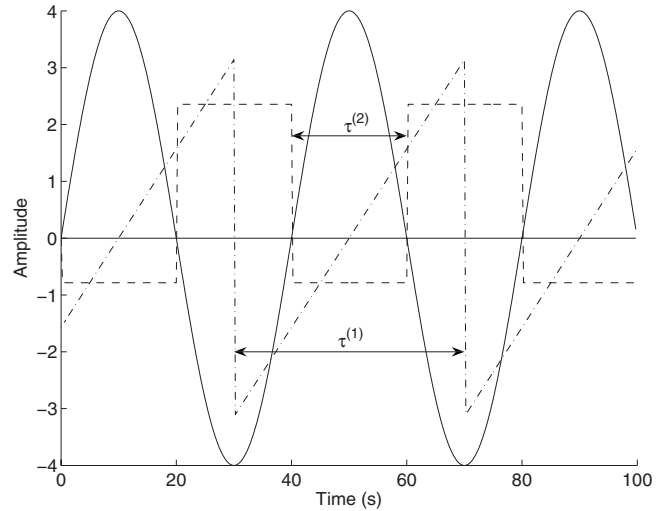

FIG. 1. Demonstration of phase slip analysis using a sine wave with a periodicity of 40 sampled at 4 Hz. The dashed line and dot-dashed line indicate the results of phase slip for $c = \pi$ and $-\pi/2$, respectively. There is a difference of $\tau^{(1)}$ sample points (corresponds to the periodicity of the sine wave) between the consecutive phase slips for $c = -\pi/2$ scenario and a difference of $\tau^{(2)}$ sample points (corresponds to half of the periodicity of the sine wave) for $c = \pi$ case. The solid line at zero running parallel to abscissa is a guide for the eyes.

duration ($\tau^{(1)}$) corresponds to a complete cycle of the signal; while for the case of π, it ($\tau^{(2)}$) corresponds to the half of the cycle of the signal. Thus, by studying the time between the successive Hilbert phase slips we can infer the periodicity of the signal. In this work, the time difference between the successive phase slips is defined as $\Delta\tau(i) = \tau(i+1) - \tau(i)$. To this end, we define a measure ρ to quantify the dynamics of the system by computing the ratio of the standard deviation of the successive time differences $\sigma(\Delta\tau)$ of the Hilbert phase slips to the percentage of slips in the data (which is the number of slips divided by the total number of points in the data). Based on the above arguments, it is straightforward to infer that for periodic signals ρ is zero $[\because\sigma(\Delta\tau)=0]$. By computing the histogram of $\Delta\tau$, it is possible to study the spectral property of the signal and this was used in earlier work to quantify the spectral property of atmospheric variables [13]. Thus, using Hilbert phase slip analysis, it is possible to study the time-dependent variations in the frequency of a signal whereas the Fourier transform characterizes the global frequency of a signal.

In order to compare the sensitivity of the Hilbert phase slip method to noise for $c = -\pi/2$ and $c = \pi$, we consider a noisy sine wave signal. We use the sine wave discussed above and simulate it for a period of 5 min with a sampling rate of 4 Hz. We also generate Gaussian distributed white noise series r with the same duration as the sine wave. We remove the average value of r and normalize its peak amplitude (to $[-1,1]$, same range as sine wave). We then add different amounts (ϵ) of the modified white noise series to the sine wave and compute $\tau^{(1)}$ and $\tau^{(2)}$. In our simulation, we vary ϵ from 0.02 to 1 in steps of 0.02. The case of noise-free scenario ($\epsilon = 0$, discussed above) serves as a base for comparison.
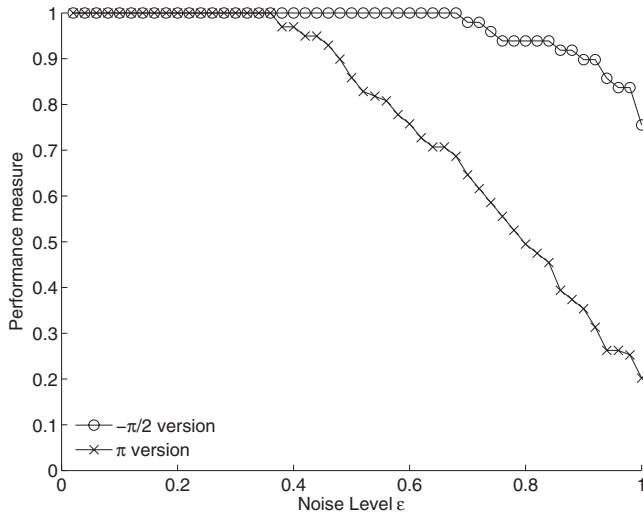
FIG. 2. Results of the performance analysis of two different phase slip ($c=-\pi/2$ and π) versions shown in Fig. 1. The performance measure is shown as a function of the noise level ϵ. The traditional Hilbert phase slip approach identifies approximately 80% of the cycles in the data correctly even when the noise level is equal to the signal level while the zero-crossing version identifies only 20% of the cycles in the data.

We define the performance measure as the ratio of the number of cycles correctly identified to the number of cycles expected. The number of cycles expected for the sine wave is calculated from the noise-free scenario. The additive noise will interfere and will change the expected values of $\tau^{(1)}$ and $\tau^{(2)}$ (which are 160 and 80 samples, respectively). To account for this variability, we consider a cycle to be correctly identified if its length is within the interval of $(1 \pm 1/8)\tau$. With this definition the performance measure will be equal to 1 if the method correctly identifies all the cycle lengths and will be equal to 0 if it does not identify any cycle length correctly.

The performance measures computed from both versions are shown in Fig. 2. It is clear that with $c=-\pi/2$ version, one can identify the periodicity of the sine wave correctly even up to $\epsilon=0.7$. Further, even with equal amount of noise ($\epsilon=1$), the $c=-\pi/2$ version identifies 80% of the cycles in the signal. Thus, the phase slip analysis with traditional Hilbert transform identifies the periodicity of the signal even in noisy situations. Though the results shown in Fig. 2 are dependent on the interval within which the cycle length is considered correct, the nature of the conclusion demonstrated in Fig. 2 will still remain the same even for a different acceptance interval. Based on this simulation result, we will use $c=-\pi/2$ to study the dynamics.

III. APPLICATION TO UNCORRELATED AND LONG-RANGE CORRELATED PROCESSES

In this section, we apply the phase slip analysis to uncorrelated and long-range correlated data to understand how effectively the method distinguishes different types of correlations. Long-range correlation (LRC) is observed in many systems ranging from DNA sequences [14], heart rate dynamics [15], and atmospheric temperature data [16]. The
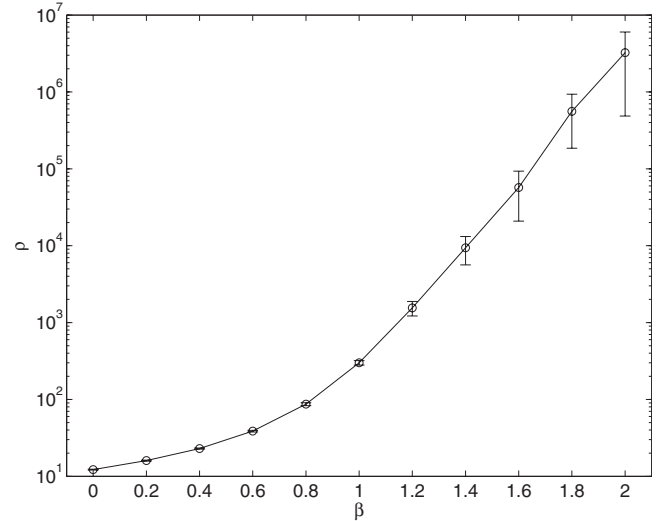

FIG. 3. Variation in ρ for uncorrelated and long-range correlated data with the magnitude of correlation dictated by the power spectral exponent β. The circles represent the mean value of ρ from 15 different realizations of a process with exponent β and the error bars indicate one standard deviation. In each realization 10^6 data points are used.

power spectrum $S(f)$ of LRC data follows a power law: $S(f) \sim f^{-\beta}$, where f is the frequency and β is the power spectral exponent. β is equal to zero for uncorrelated data while it is positive for LRC data and negative for anticorrelated data. LRC data can be synthesized retrospectively using the Fourier filtering approach by introducing the desired correlation to Gaussian white noise in the Fourier domain as follows: $F^{-1}\{P(f)f^{-\beta/2}\}$, where $P(f)$ is the Fourier transform of the Gaussian white noise [17]. In this work, we synthesize different data sets with β ranging from 0 to 2 in steps of 0.2. For each β we synthesize 15 different realizations and apply phase slip analysis. The mean value of ρ from all the different realizations and the standard deviations are shown in Fig. 3 as a function of β.

It is evident from Fig. 3 that Hilbert phase analysis is able to clearly distinguish different types of LRC data with β ranging from 0 to 1.2. For β value 1.3 and above there is a considerable overlap between them. For these values of β the data fall into the realm of nonstationary. As Hilbert transform is computed using Fourier based approach, the latter cannot perform better on the nonstationary data. Thus, the Hilbert phase is not well definable for these data sets and hence the approach is not able to clearly distinguish them. Based on the return interval analysis, LRC data can be thought of as clusters of small and large fluctuations [18]. The return times of these clusters increase with the increase in the magnitude of correlation (i.e., β). The case of white noise is a high-frequency process and hence will have large number of slips in a given period of time. Therefore, the time interval between successive phase slips will be short and the ρ will be small. However, for larger correlations (β), low-frequency components will dominate and the time interval between successive phase slips will increase and we will observe a positive trend of ρ versus β dependence.
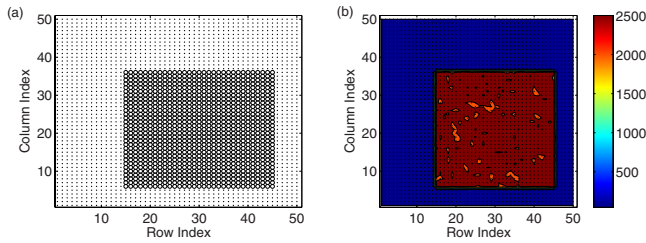
FIG. 4. (Color online) Results of the phase slip analysis of AR2 process on a square lattice. (a) A 50×50 square lattice in which each lattice point is modeled as AR2 process. The lattice points marked with thin dots and circles are modeled with ($a_1 = 1.35, a_2 = -0.14$) and ($a_1 = 2, a_2 = -0.98$), respectively. For each lattice point we simulate 10^6 points. (b) Contour map of ρ of the AR2 process from each lattice point. Phase slip analysis clearly distinguishes the two distinct AR2 processes introduced in the lattice.

IV. APPLICATION TO SPATIOTEMPORAL AR2 LATTICE MAP

In this work we apply the phase slip analysis to the spatiotemporal neonatal and fetal magnetoencephalography (MEG) data. Hence, we first test this approach on a simulated spatiotemporal system. For this purpose we consider a 50×50 lattice and model each lattice point by an independent AR2 process. Traditionally, an AR2 process has been thought of as a stochastic harmonic oscillator characterized by two parameters, the periodicity T and the decay time τ. Mathematically an AR2 process y is defined as follows: $y[n] = a_1 y[n-1] + a_2 y[n-2] + \eta[n]$, where η is the Gaussian white noise, which drives the system. a_1 and a_2 are the parameters of AR2 process and are defined as follows: $a_1 = 2 \cos(2\pi/T) e^{-1/\tau}$ and $a_2 = e^{-2/\tau}$.

The AR2 process has been traditionally used to model the biological systems such as tremors [19], brain dynamics [20–22], and atmospheric variability [23]. Here we model the lattice points using the AR2 model with $\tau = 1$ and $T = 1$, which we define as scenario 1 and a subset of lattice points using $\tau = 80$ and $T = 80$, which we define as scenario 2 and these are shown in Fig. 4(a). The primary objective of this simulation is to mimic a spatiotemporal setting analogous to our multichannel sensor environment involved in acquiring fetal and neonatal brain signals.

Phase slip analysis is performed on the data from each lattice point and the result for the lattice model is given in Fig. 4(b). The two scenarios that are modeled with different sets of parameters are clearly distinguished. In scenario 1, the parameters are close to zero and the AR2 has characteristics of white noise while in scenario 2 the parameters are largely deviated from zero and hence AR2 has strong oscillatory characteristics. Based on the above arguments and from the knowledge of the phase slip analysis of short and LRC data (see Fig. 3), one would expect a low ρ for scenario 1 compared to scenario 2 and this is observed in our simulation [see Fig. 4(b)]. It is important to note that the unit of $\Delta\tau$ is in steps for the LRC and white noise data and for the AR2 data as well and hence ρ is in the units of (iteration) steps whereas when applied to continuous system the unit of $\Delta\tau$ will be in seconds and hence the unit of ρ will be in seconds.

V. APPLICATION TO NEONATAL AND FETAL MEG

In this section, we apply the phase slip analysis to spatiotemporal neonatal and fetal MEG data to localize the sensors containing the spontaneous brain activity (SBA). Neonatal and fetal MEG is recorded using an instrument called SARA (SQUID Array for Reproductive Assessment), which is designed and installed at the University of Arkansas for Medical Sciences specifically to study the maternal-fetal electrophysiology. This instrument is completely noninvasive and detects weak biomagnetic fields associated with the electrophysiological activity in the human body [24]. SARA is equipped with 151 primary magnetic sensors with an approximate distance between the sensors of 3 cm and spread over an area of 1300 cm^2. The sensor array spans the maternal abdomen longitudinally from the symphysis pubis to the uterine fundus and a similar distance laterally.

Traditionally, fetal brain evoked response is used to understand the neurological maturation of the fetus [25,26]. Typically in fetuses, for an auditory and visual response study using SARA, an ultrasound measurement is performed prior to the study to locate the fetal head position and the same is marked using a coil (head coil) attached to maternal abdomen. Based on this measurement, the distal end of the (auditory or visual) stimulator is placed on the maternal abdomen in the area overlaying the fetal head. As most of the evoked responses are confirmed by visual inspection, the knowledge of the fetal head region gained through ultrasound measurements will also help to trace the evoked responses around the same region in the sensor domain [25,27].

In addition to the evoked response, the neurological maturation can also be studied with the SBA [28]. The classical patterns in SBA such as tracé alternant (TA), continuous, and tracé discontinuous patterns are indicative of sleep-wake cycles that change with gestational age [29] and help to understand the neurological maturation. The feasibility of measuring SBA and identifying these classical patterns in newborns [30] and fetuses [31] using SARA have been demonstrated recently. In the case of an evoked response study, the response from a sensor that overlaps with the ultrasound measurement provides a secondary confirmation that the response is of cortical (brain) origin. However, in the case of SBA, a larger group of sensors that may contain the fetal brain signals is selected based on the ultrasound measurement. The brain patterns are usually scored by visual inspection and the scoring process is more difficult if the scorer has to deal with many sensors. Thus, an automated approach that limits the number of possible sensors that may contain the SBA will make the scoring process easier. We propose to use the phase slip analysis to identify the sensors that may contain SBA.

Our problem is to distinguish the sensors that contain SBA from others in the noise floor. However, we would like to mention that the MEG channel noise (which is sensor noise plus environment noise) will not have the same broadband spectrum as the computer generated white noise (that are discussed in Figs. 3 and 4). Further, the preprocessing steps such as a digital filter will change the spectral property of the channel noise. In the case of fetal MEG, the environ-
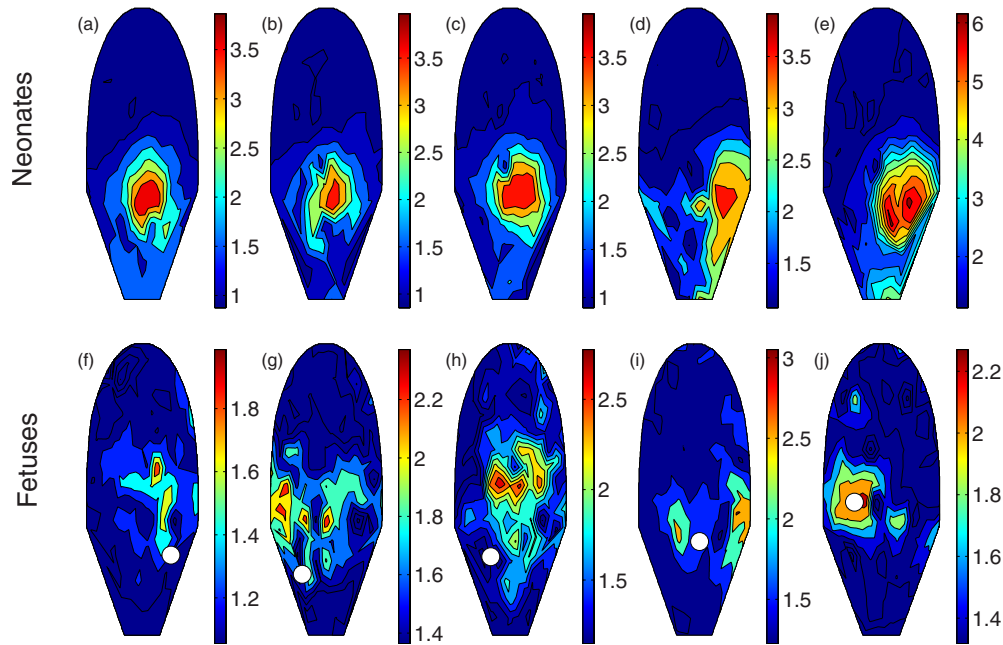
FIG. 5. (Color online) Results of the phase slip analysis of neonatal and fetal MEG data presented on the SARA sensors. A contour plot of ρ of the neonatal and fetal MEG is shown in (a)–(e) and (f)–(j), respectively. The phase slip analysis clearly highlights the sensors overlaying the (neonatal-fetal) brain area. In (f)–(j), the fetal head region marked using ultrasound is shown as a white dot. For the sake of clarity, the results are presented in different magnitudes. For each data an estimate of ρ for background is obtained by calculating the median value of ρ obtained for the signals from the sensors on the boundary of the SARA system and this value is set as a lower bound in each map. The distance from top to bottom of each graph is 45.3 cm and the distance between the widest section of the graph is 33.3 cm.

mental noise includes other biological signals that are pertinent to the fetal development such as maternal and fetal breathing, maternal-fetal cardiac signals, uterine contractions, etc. The breathing artifacts and the uterine contractions are low-frequency processes and can be attenuated using appropriate (low-pass) filter. The cardiac signals are attenuated using signal space projection (SSP) technique [32]. If the intensity of the interfering source is minimal and stationary (e.g., includes minimal to no fetal motion during the recording) then they are attenuated properly or else the partially attenuated interference will contribute to the MEG channel noise [33]. The MEG channel noise is commonly called background activity. Hence, our actual problem is to distinguish the sensors that contain SBA from the sensors that contain background activity.

In the case of newborns, the sensors on which the newborn head is rested can be easily determined during the study (usually middle and lower sensors) and hence the SBA analysis can be restricted only to those sensors. Thus, neonatal MEG data can serve as a good test bed for our algorithm before we apply it to the fetal MEG data. We consider five neonatal MEG data. Further, we consider five fetal MEG data recorded in the following gestational ages: 31 week, 33 week, 34 week, and two in 36 week. For details of the recording procedure we refer elsewhere [25]. MEG is collected using SARA with a sampling rate of 312.5 Hz for a period of 6 min. The interfering cardiac signals are removed by the SSP technique [29,30] and the data are band pass filtered (0.5–25 Hz) [30] using the Butterworth filter with zero phase distortion.

Phase slip analysis is performed for the MEG from each SARA sensor and the ρ computed is shown on the SARA

sensor domain as a contour map (see Fig. 5). Figures 5(a)–5(e) represent the results of the neonates and Figs. 5(f)–5(j) represent the results of the fetal data sets. In the case of neonates, after the removal of the cardiac signal, the dominant signal left will be the brain activity. Hence, one would expect the signals to be localized only over a few sensors on which the neonate head is positioned and the rest of the sensors to be populated with signals due to the background activity, which in the neonatal case is just SARA noise floor (usually less than $5fT/\sqrt{Hz}$).

As the neonatal brain signals are shown to be a band limited process (0.5–25 Hz) exhibiting spectral (δ, θ, α, and β) activities [34], the sensors containing brain signals are expected to show higher ρ values compared to the rest (analogous to AR2 lattice scenario). This is indeed observed for all the neonatal data [see Figs. 5(a)–5(e)].

Fetal MEG is more complicated than neonatal MEG. Fetal MEG measured using SARA is a superposition of maternal-fetal cardiac signals and fetal brain activity. As mentioned above, it will contain other biological signals that are related to the fetal development. The dominant interference is caused by fetal motion. If the fetal motion during the SARA study is large, the fetal brain signals will be dispersed to a large number of sensors.

A fetal movement study is often done using an ultrasound measurement. With the current technology it is difficult to perform an ultrasound measurement in parallel to the SARA study [35]. However, it is possible to understand the fetal movement by analyzing the fetal heart rate and actogram, which is the variation in R-wave amplitude, a dominant component of cardiogram, with time [36]. This analysis can be readily performed using the fetal cardiogram, which is ob-
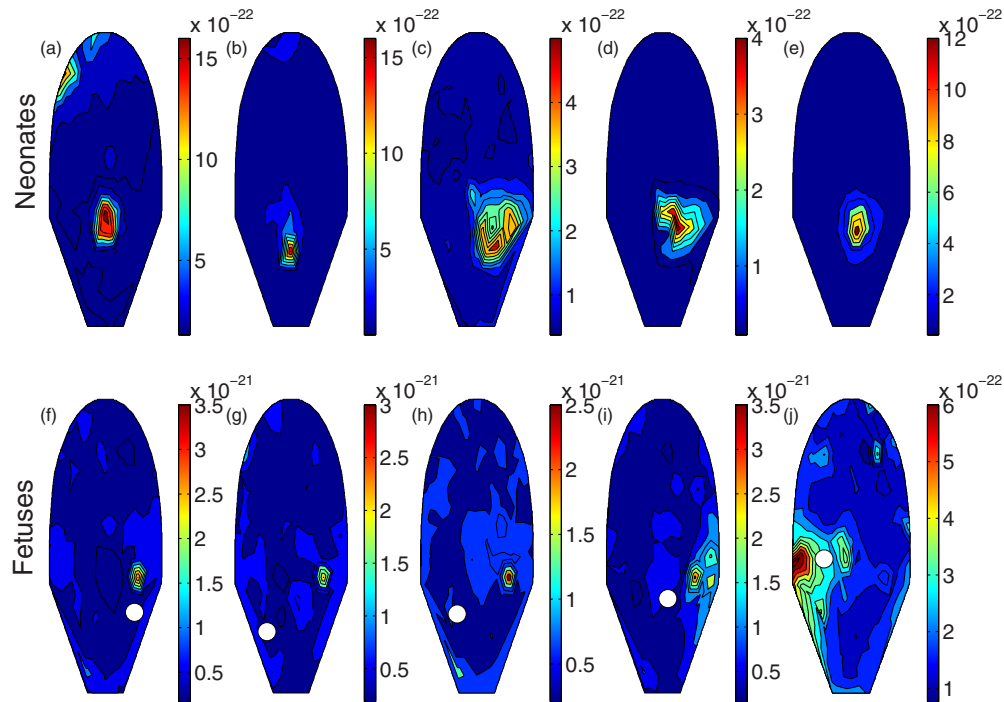
FIG. 6. (Color online) Results of the power spectral analysis of neonatal and fetal MEG data presented on the SARA sensors. A contour plot of the median value of spectral power in 0.5–25 Hz of the neonatal and fetal MEG is shown in (a)–(e) and (f)–(j), respectively. In the case of neonates, the phase slip approach and the power spectral yield similar results. However, for fetuses the power spectral approach localized an incorrect region. In (f)–(j), the fetal head region marked using ultrasound is shown as a white dot. For the sake of clarity, the results are presented in different magnitudes.

tained as a by-product in the SARA measurement. The actogram and the fetal heart rate variability analyses confirmed the presence of the fetal movements in the data sets discussed here. The actogram and heart rate are not presented here as they are beyond the scope of the current work.

Because of this motion, we observe a larger spread of the fetal brain signals in Figs. 5(f)–5(j). Further, similar to neonates, fetal brain signals are also shown to be a band limited process (0.5–25 Hz) [31] and hence the sensors containing fetal brain signals are expected to have higher ρ values compared to the rest [see Figs. 5(f)–5(j)]. Except for the fetus shown in Fig. 5(h), the results of phase slip analysis in all other fetuses qualitatively match with the sensor region marked by the ultrasound measurement [shown in white dots in Figs. 5(f)–5(j)].

In order to get an estimate of the phase slip metric (ρ) for background activity of the SARA signals, one can collect SARA data from nonpregnant women and perform the Hilbert phase analysis. However, the use of biological surrogates (mothers) has been questioned [37] and hence we follow the data-driven approach. For this purpose we consider the signals from the sensors on the boundary of the SARA system. These sensors usually do not contain any signal pertinent to fetal brain activity. We compute median value of ρ obtained for these signals and use it as the estimate of background activity. In Fig. 5, we set this value as a lower bound for the contour map.

Based on the spectral property (limited to 0.5–25 Hz) of the neonatal and fetal MEG data, it may appear straightforward to use the simple power spectral approach to identify

the sensors containing SBA. To examine this further, we compute the median power in 0.5–25 Hz for all MEG sensors and present the results in Fig. 6. Figures 6(a)–6(e) represent the results of the neonates and Figs. 6(f)–6(j) represent the results of the fetuses. The results of neonates shown in Figs. 6(b)–6(d) agree very well with the phase slip metric shown in Figs. 5(b)–5(d). In Fig. 6(a) though the dominant activity shown in the lower part of the sensor matches with the results in Fig. 5(a), the spectral analysis has spuriously identified activities in the top sensors [see Fig. 6(a)].

In general, the order of magnitude of SARA signals varies as follows: closer to the maternal heart, the maternal cardiac signals can be as large as 100 picotesla (pT); the fetal cardiac signal can be as large as 10 pT at the fetal thorax position; near the head region the fetal brain signals can be as large as 500 fT and the neonatal brain signals can be as large as 1000 fT. Based on these details, any measure that we use to quantify the brain signals should yield a higher (or equal) value for neonates than the fetuses. For fetuses, the phase slip metric shown in Figs. 5(f)–5(j) is in the same range or lower than the values exhibited by the neonates [see Figs. 5(a)–5(e)]. These results corroborate the above argument based on the signal strengths of the fetal and neonatal brain signals. However, the median value of the spectral power of the fetal MEG shown in Figs. 6(f)–6(i) is larger than the neonates. The result of the fetus shown in Fig. 6(j) is almost in the same range as the neonates and in this case both the phase slip metric and spectral results have localized almost the same region while in the other fetuses the spectral approach has localized an entirely different region. The magni-

tude of the strongest signals identified in Figs. 6(f)–6(i) is too high to attribute them to fetal brain signals and hence they must correspond to the fetal heart residue. The difference in the spatial locations of the strongest signals [see Figs. 6(f)–6(i)] identified by the spectral approach compared to the phase slip approach [Figs. 5(f)–5(i)] also supports the fact that these locations correspond to fetal cardiac signals. Thus, the fetal brain signals can be reliably identified using the phase slip approach compared to the traditional spectral approach.

Qualitatively, the neonates have higher ρ values compared to the fetuses (see Fig. 5) indicating that the MEG power in neonates is higher than fetuses. However, the minimum value of ρ in both groups varies between 0.4–0.5 s. To understand the performance range of our approach, we computed the root-mean-square value of sensors that exhibited the highest ρ in all the data sets reported in Fig. 5. This analysis showed that the sensor signals should be in the range of about 70 fT and above for this approach to be able to detect it. This conclusion also agrees with the results in Fig. 2, which loosely indicate that the Hilbert phase slip will be able to correctly identify signals whose amplitude is roughly comparable to the peak-to-peak noise amplitude. In the present case, the peak-to-peak sensor noise amplitude is approximately 100 fT, which is in rough agreement with the 70 fT amplitude estimated from the data.

To ascertain the SBA identified using our approach, we present in Fig. 7 the neonate and fetal MEG traces, one each from the regions of high and low ρ. These traces correspond to the data sets shown in Figs. 5(a) and 5(j). It would be difficult to distinguish (except for the amplitude) between the SBA and signal in the noise floor of SARA if we presented the traces from the whole study. Instead, we present the MEG traces that contain TA activity (scored by the expert neurologist) for a neonate and a fetus in Figs. 7(a) and 7(c), respectively. Further, we also present Figs. 7(b) and 7(d) for comparison of the data from a sensor that has low ρ in the same time duration as shown in Figs. 7(a) and 7(c). The traces shown in Figs. 7(a) and 7(c) have burst and quiescent periods which are common features of TA while the traces shown in Figs. 7(b) and 7(d) lack these characteristics indi-
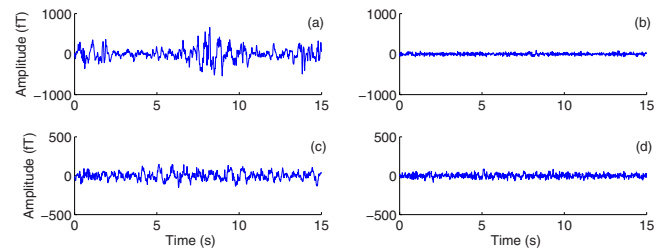

FIG. 7. (Color online) Time traces of MEG from the neonate (a), (b) and the fetus (c), (d) discussed in Figs. 5(a) and 5(j), respectively. (a) and (c) MEG traces from sensors with highest ρ. (b) and (d) MEG traces in the same time duration as shown in (a) and (c) but from sensors with lowest ρ. See text for details.

cating that they are not SBA. This clearly shows that our approach is able to localize the SBA in fetal MEG.

VI. CONCLUSION

Using Hilbert phase analysis we could clearly distinguish the dynamics of different types of data ranging from uncorrelated noise to color noise. Further, by applying to a spatiotemporal AR2 lattice, we could demonstrate that the phase slip analysis distinguishes two regimes that are modeled with different sets of AR2 parameters. Finally, by extending this approach to the neonatal and fetal MEG data, we have demonstrated that this method is able to reliably localize the (sensor) regions that contain the brain activity. In future work, the brain signals identified using this approach will be analyzed for the classical brain patterns in SBA to understand the neurological maturation of the fetus. Further, the generalized Hilbert transform introduced in this work may open a lot of venues for theoretical advancements in the field.

[1] G. E. P. Box, *Time Series Analysis: Forecasting and Control* (Prentice-Hall, Englewood Cliffs, NJ, 1994).

[2] P. Tass, M. G. Rosenblum, J. Weule, J. Kurths, A. Pikovsky, J. Volkmann, A. Schnitzler, and H. J. Freund, Phys. Rev. Lett. **81**, 3291 (1998).

[3] L. Xu, Z. Chen, K. Hu, H. E. Stanley, and P. C. Ivanov, Phys. Rev. E **73**, 065201(R) (2006).

[4] M. Palus and A. Stefanovska, Phys. Rev. E **67**, 055201(R) (2003).

[5] N. B. Janson, A. G. Balanov, V. S. Anishchenko, and P. V. E. McClintock, Phys. Rev. Lett. **86**, 1749 (2001).

[6] N. B. Janson, A. G. Balanov, V. S. Anishchenko, and P. V. E. McClintock, Phys. Rev. E **65**, 036211 (2002).

[7] J. Gross, P. A. Tass, S. Salenius, H. J. Freund, and A. Schnit-

zler, J. Physiol. **527**, 623 (2000).

[8] D. M. Halliday, J. R. Rosenberg, A. M. Amjad, P. Breeze, B. A. Conway, and S. F. Farmer, Prog. Biophys. Mol. Biol. **64**, 237 (1995).

[9] M. A. Zaks, E. H. Park, M. G. Rosenblum, and J. Kurths, Phys. Rev. Lett. **82**, 4228 (1999).

[10] E. H. Park, M. A. Zaks, and J. Kurths, Phys. Rev. E **60**, 6627 (1999).

[11] S. Boccaletti, J. Kurths, G. Osipov, D. L. Valladares, and C. S. Zhou, Phys. Rep. **366**, 1 (2002).

[12] B. Kedem, Proc. IEEE **74**, 1477 (1986).

[13] D. Rybski, S. Havlin, and A. Bunde, Physica A **320**, 601 (2003).

[14] C. K. Peng, S. Buldyrev, A. Goldberger, S. Havlin, F. Scior-

tino, M. Simons, and H. E. Stanley, Nature (London) **356**, 168 (1992).

[15] C. K. Peng, S. Havlin, H. E. Stanley, and A. L. Goldberger, Chaos **5**, 82 (1995).

[16] E. Koscielny-Bunde, A. Bunde, S. Havlin, H. E. Roman, Y. Goldreich, and H. J. Schellnhuber, Phys. Rev. Lett. **81**, 729 (1998).

[17] J. Timmer and M. Konig, Astron. Astrophys. **300**, 707 (1995).

[18] A. Bunde, J. F. Eichner, S. Havlin, and J. W. Kantelhardt, Physica A **342**, 308 (2004).

[19] J. Timmer, M. Lauk, W. Pfleger, and G. Deuschl, Biol. Cybern. **78**, 349 (1998).

[20] L. Zetterberg, Math. Biosci. **5**, 227 (1969).

[21] P. B. C. Fenwick, P. Mitchie, J. Dollimore, and G. W. Fenton, Agressologie **10**, 553 (1969).

[22] W. Gersch, *Handbook of Electroencephalography and Clinical Neurophysiology* (Elsevier, Amsterdam, 1987), p. 261.

[23] D. Maraun, H. W. Rust, and J. Timmer, Nonlinear Processes Geophys. **11**, 495 (2004).

[24] H. Eswaran, H. Preissl, J. D. Wilson, P. Murphy, S. E. Robinson, and C. L. Lowery, Am. J. Obstet. Gynecol. **187**, 145 (2002).

[25] M. Holst, H. Eswaran, C. Lowery, P. Murphy, J. Norton, and H. Preissl, Clin. Neurophysiol. **116**, 1949 (2005).

[26] E. Schleussner, U. Schneider, S. Kausch, C. Kaehler, J.

Haueisen, and H. J. Seewald, Br. J. Obstet. Gynaecol. **108**, 1291 (2001).

[27] R. Draganova, H. Eswaran, P. Murphy, M. Huotilainan, C. Lowery, and H. Preissl, Neuroimage **28**, 354 (2005).

[28] M. S. Scher, D. A. Steppe, and D. L. Banks, Sleep **18**, 531 (1995).

[29] M. S. Scher, D. A. Steppe, R. E. Dahl, S. Asthana, and R. D. Guthrie, Sleep **15**, 442 (1992).

[30] N. Haddad, B. Shihabuddin, H. Preissl, M. Holst, C. L. Lowery, and H. Eswaran, Clin. Neurophysiol. **117**, 289 (2006).

[31] H. Eswaran, N. I. Haddad, B. S. Shihabuddin, H. Preissl, E. R. Siegel, P. Murphy, and C. L. Lowery, Clin. Neurophysiol. **118**, 1940 (2007).

[32] J. Vrba, S. E. Robinson, J. Mccubbin, C. L. Lowery, H. Eswaran, J. D. Wilson, P. Murphy, and H. Preissl, IEEE Trans. Biomed. Eng. **51**, 1207 (2004).

[33] J. Vrba, S. E. Robinson, J. Mccubbin, P. Murphy, H. Eswaran, J. D. Wilson, H. Preissl, and C. L. Lowery, Neuroimage **21**, 1009 (2004).

[34] H. Eswaran and D. F. Rose, Exp. Neurol. **190**, S37 (2004).

[35] H. Zhao, M. Chen, B. D. Van Veen, J. F. Strasburger, and R. T. Wakai, IEEE Trans. Biomed. Eng. **54**, 1167 (2007).

[36] H. Zhao and R. T. Wakai, Phys. Med. Biol. **47**, 839 (2002).

[37] M. Thiel, M. C. Romano, J. Kurths, M. Rolfs, and R. Kliegl, Europhys. Lett. **75**, 535 (2006).